Weak bonding of alumina coatings on Ni(1 1 1)

Emily A.A. Jarvis, Asbjorn Christensen, Emily A. Carter *

Department of Chemistry and Biochemistry, Box 951569, University of California, Los Angeles, CA 90095-1569, USA

Abstract

We examine the structure and stability of an ultrathin ceramic film coating a metal substrate, specifically, an α-alumina, Al_2O_3, film grown on fcc nickel. This metal–ceramic interface may play a role in materials failure of current combustion engine thermal barrier coatings (TBC's). We characterize the (0 0 0 1) surface of α-Al_2O_3 and study the effect of increasing alumina film thickness on the alumina/nickel interface using periodic slab density functional theory within the generalized gradient approximation. Since Ni forms stable alloys with Al, it is not obvious whether the bonds between Ni and alumina will be Ni–Al, Ni–O, or both. Interestingly, our calculations indicate that the preferred bonding mode depends on the thickness of the alumina film. Namely, for one monolayer of alumina, the alumina appears amorphous and both Ni–O and Ni–Al interactions take place, while for two and three monolayers, Ni–O interactions decrease and Ni–Al bonds become more pronounced. By studying the effect of increasing alumina thickness on the Ni substrate, we observe a marked decrease in the work of adhesion for thicker alumina coatings. This provides a new atomic-scale explanation for the observed increase in spallation with increasing thickness of oxide layer (alumina) that forms during preparation and operational cycling of TBC's. The thickest alumina layers energetically prefer intra-ceramic bonding over Al_2O_3/Ni interface formation. Connections to metal catalyst–oxide support interfaces are also discussed. © 2001 Elsevier Science B.V. All rights reserved.

Keywords: Density functional calculations; Metal–insulator interfaces; Ceramics; Aluminum oxide; Nickel; Coatings

1. Introduction

Interfaces between metals and ceramics arise in numerous practical applications, including electronics, heterogeneous catalysis, oxidized alloys, electrochemical fuel cells, gas sensors, and thermal protective coatings. From a more fundamental standpoint, these interfaces are interesting simply because they are poorly characterized and their intrinsic nature at the atomic level is poorly un-derstood. Experimental techniques to probe such interfaces have advanced such that spatially-resolved, high-resolution characterization of internal interfaces is possible for select cases. At the same time, increased computational power allows simulation of larger, more realistic systems. Accordingly, the characterization of heterogeneous materials interfaces has increasingly become a topic of intense research efforts over the past decade.

A number of experimental techniques for measuring interfacial binding exist in the literature. Gupta et al. developed a measure of interface strength whereby a laser pulse is converted to a pressure pulse sent through the substrate towards

---

* Corresponding author. Fax: +1-310-267-0319.
  E-mail address: eac@chem.ucla.edu (E.A. Carter).

				Form Approved
Report Documentation Page				*OMB No. 0704-0188*

Public reporting burden for the collection of information is estimated to average 1 hour per response, including the time for reviewing instructions, searching existing data sources, gathering and maintaining the data needed, and completing and reviewing the collection of information. Send comments regarding this burden estimate or any other aspect of this collection of information, including suggestions for reducing this burden, to Washington Headquarters Services, Directorate for Information Operations and Reports, 1215 Jefferson Davis Highway, Suite 1204, Arlington VA 22202-4302. Respondents should be aware that notwithstanding any other provision of law, no person shall be subject to a penalty for failing to comply with a collection of information if it does not display a currently valid OMB control number.

1. REPORT DATE **APR 2001**	2. REPORT TYPE	3. DATES COVERED **00-00-2001 to 00-00-2001**

4. TITLE AND SUBTITLE **Weak bonding of alumina coatings on Ni(111)**	5a. CONTRACT NUMBER
	5b. GRANT NUMBER
	5c. PROGRAM ELEMENT NUMBER
6. AUTHOR(S)	5d. PROJECT NUMBER
	5e. TASK NUMBER
	5f. WORK UNIT NUMBER

7. PERFORMING ORGANIZATION NAME(S) AND ADDRESS(ES) **University of California, Los Angeles,Department of Chemistry and Biochemistry,Box 951569,Los Angeles,CA,90095-1569**	8. PERFORMING ORGANIZATION REPORT NUMBER
9. SPONSORING/MONITORING AGENCY NAME(S) AND ADDRESS(ES)	10. SPONSOR/MONITOR'S ACRONYM(S)
	11. SPONSOR/MONITOR'S REPORT NUMBER(S)

12. DISTRIBUTION/AVAILABILITY STATEMENT
Approved for public release; distribution unlimited

13. SUPPLEMENTARY NOTES

14. ABSTRACT

15. SUBJECT TERMS

16. SECURITY CLASSIFICATION OF:			17. LIMITATION OF ABSTRACT	18. NUMBER OF PAGES	19a. NAME OF RESPONSIBLE PERSON
a. REPORT **unclassified**	b. ABSTRACT **unclassified**	c. THIS PAGE **unclassified**	**Same as Report (SAR)**	**22**	

Standard Form 298 (Rev. 8-98)
Prescribed by ANSI Std Z39-18

the coating interface. The reflected tensile wave from the coating free surface results in spallation (deadhesion). The critical stress amplitude that accomplishes the spallation can be determined via computer simulation. This technique also has the ability to determine interfacial toughness for certain systems [1,2]. Similar spallation techniques have been employed by other groups [3,4] and have been used by Gupta et al. to measure the tensile strength of interfaces at elevated temperatures [5]. Thin film multiple cracking [6] and tensile stress–strain measures of metal–ceramic single fibers [7] can also be used to measure interfacial shear strengths; however, the stress–strain single fiber study determined shear strengths that were an order of magnitude lower than those obtained by the multiple cracking technique [7]. Forms of micro-indentation tests as a measure of interfacial shear strength are useful [8,9], but inhomogeneities may require numerous measurements of this type to really obtain a representative sampling of the interface. Conversely, direct pull measures are also used to measure interfacial adhesion in ceramic–ceramic [10] and metal–ceramic [11] systems. Continuous microscratch techniques are able to provide a qualitative measure of adhesion strengths in metal–ceramic and other bi-material systems [12,13]. Likewise, adhesion strengths for metal–ceramic interfaces can be measured via particle profiles for solid–solid interfaces [14] or the contact angle that a drop of metal makes with the substrate [15]. Interfacial toughness can also be investigated by four point bending tests calibrated via finite element analysis [16] and by delamination measurements of residually stressed coatings deposited over the thin film interface [17]. More recently, micro-calorimetry measures of metal adhesion on oxide thin film surfaces have been performed, which provide estimates of bulk adhesion energetics [18]. A study by Ashcroft and Derby employed five different measures of adhesion and found that no test was able to provide quantitative adhesion measures, although all tests provided the same adhesion strength ordering of the samples [19]. Thus, although experimental techniques are able to provide qualitative measures of adhesion between metal–ceramic interfaces, quantitative results are generally difficult or impossible to obtain.

A plethora of inherent difficulties arise when attempting to experimentally measure the intrinsic strengths of interfaces. The elusiveness and irreproducibility of quantitative measurements in this field are primarily caused by the presence of imperfections (defects, voids, etc.) created upon sample preparation. It is virtually impossible to create an ideal interface and to reproducibly measure the work of separation (adhesion strength) of such an interface. As a result, we have begun a series of first-principles theoretical studies designed to characterize the adhesion and bonding at ideal interfaces between ceramics and metals [20–22]. Concurrent with these studies, we also are investigating specific effects of reduction [23] and oxidation [24] on materials properties and failure. Of course, such calculations isolate the atomic-level interactions and cannot account for certain long-ranged relaxation effects and dislocation/defect emission mechanisms for energy dissipation present in physical fracture measurements. Accordingly, the adhesion values presented here may generally predict a "lower bound" on the interface adhesion.

1.1. Metal–ceramic interfaces of thermal barrier coatings

The thermal barrier coatings (TBC's) used in airplane jet engine turbines provide a practical example where optimization of metal–ceramic interfaces is crucial. Similar materials technology is used in such diverse applications as coating the gas turbines of stationary power plants to creating protective outer coatings for the space shuttle! What all such applications have in common is the necessity of a protective coating designed to withstand the harsh temperature cycling and the potentially oxidative/corrosive operating environment.

During operation, jet engine components are exposed to harsh cycles of heating and cooling, spanning a temperature range in excess of 1400 K. TBC's are designed to protect the metal superalloy of an engine from these extremely high temperatures associated with combustion. An optimal TBC must possess a well-matched structure to that of the substrate and maintain this by similar

thermal expansion over the entire range of temperatures accessed during the thermal cycling. It must also be designed to have favorable adhesion to the substrate and very low thermal conductivity. In fact, the thermal conductivity of zirconia, the favored ceramic for turbine protective coatings, is so low that even a coating less that one millimeter thick can reduce the effective temperature to which the underlying metal superalloy is exposed by several hundred degrees Celsius [25]! In modern jet engines, the operating temperature often *exceeds* the melting points of the metal alloy components. Accordingly, it is essential that the TBC maintain its uninterrupted protective barrier.

A schematic structure of a thermal barrier coating is shown in Fig. 1. The substrate is a nickel-based alloy of macroscopic thickness. A common metal alloy bond coat for nickel-alloy substrates consists of Ni with Cr, Al, and Y and is generally ~100–150 μm thick [26]. The bond coat composition may replace or decrease the amount of Ni to add Fe and Co, especially in the case of steel substrate applications [27,28]. This bond coat promotes adhesion and is designed to serve as a gradation layer for thermal expansion coefficient mismatch between the top coat and substrate. Because the yttria-stabilized-zirconia top coat is essentially transparent to oxygen ion diffusion at high temperatures, an unintended thermally grown oxide (TGO) layer, consisting primarily of Al_2O_3, thickens with repeated thermal cycling [29]. Although the TGO is not intentionally fabricated as part of the TBC, such a layer is anticipated and

provides some protection against oxidation of the underlying alloy, since oxygen does not readily diffuse through alumina. Al_2O_3 generally forms even prior to thermal cycling, due to the conditions present in the deposition chambers where the TBC's are prepared. With repeated thermal cycling, the TBC experiences failure in the form of spallation (chipping off the substrate); the TGO may be partially responsible for this failure [30,31].

TBC spallation is a well-known problem that has been studied by a number of experimental and theoretical techniques. Quantitative linking of theory to experimental findings has proven difficult. Several aspects of TBC failure studies pose difficulties from a theoretical standpoint: the large length-scales of the phenomenon (e.g., cracking can occur on the micron scale or larger), numerous small percentage-component "contaminants" or "dopants" in pure metals and ceramics, time scales associated with failure evolution that are much longer than characteristic atomic-level dynamics, and the harsh oxidative/corrosive environment and repeated cycling through a wide temperature range. To be computationally feasible, theoretical studies must purposefully ignore at least some of these complications. Ab initio calculations are computationally expensive, which generally limits their applicability to systems of ~100 atoms. This limits the chemical and physical complexity of the interface system that can be explored. However, a first-principles approach has the advantage of being parameter free, i.e. the atomic interactions are "unbiased" – an especially useful feature for
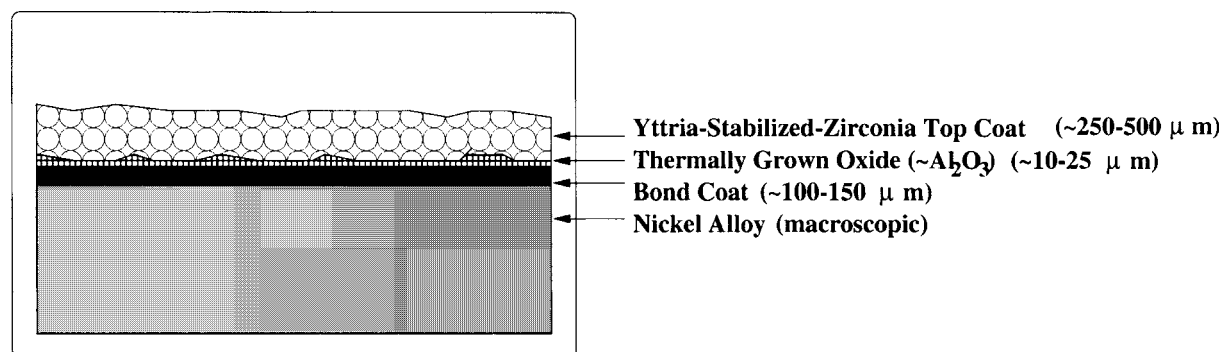

Fig. 1. Cross-section of a TBC.

situations where fundamental interactions are poorly understood. Accordingly, we perform first-principles density functional theory (DFT) calculations to characterize an ideal interface between the metal alloy bond coat and the TGO to explore possible atomic-level causes of spallation. Naturally, it is likely that the real interfaces present in the TBC are considerably more complicated than the model Al_2O_3/Ni interface presented here. Since the exact structure and composition at the interface is not well-characterized experimentally, we believe a study of the ideal interface between stoichiometric alumina and nickel is a useful first-order approximation to the physical interface and presents valuable insight into the atomic-scale interactions present at an interface with such a chemical composition.

1.2. Choice of interface matching

At low temperatures, a variety of "transitional" forms of alumina exist. These transitional forms cannot be considered true polymorphs of corundum, α-alumina; heating transformations between these forms are not reversible [32]. Upon heating, thermally-formed oxides of metallic aluminum transform from γ-alumina into the corundum, α-alumina, structure. This transformation may occur from ∼1173 to 1373 K, well within the temperature range inside an operating jet engine. The corundum crystals have been shown to grow with the basal, (0 0 0 1), plane oriented parallel to the surface for thin films [33]. Since we are interested in the system where alumina "grows" on the bond coat alloy, we chose to model the basal plane in our calculations. Previous first-principles DFT [34,35] and semi-empirical studies [36] have shown the (0 0 0 1) plane to be one of the most energetically favorable surfaces of alumina. These theoretical predictions and observation that the (0 0 0 1) face of α-Al_2O_3 grows in during high temperature oxidation of metallic aluminum motivate our investigation of this surface, despite the fact that achieving ideal cleavage along this direction may be difficult or impossible [37].

In this paper, we concentrate on the interface formed between alumina and nickel; specifically, the α-Al_2O_3(0 0 0 1)/Ni(1 1 1) interface. Some de-

bate regarding the optimal planes to match cubic metals with the basal plane of α-alumina is present in the literature. Simple arguments based on surface energy gain with interface formation led to conjecture that the (1 1 0) plane should be most favorably joined with the (0 0 0 1) plane of alumina [38]. However, vapor-deposition experiments of Ni on a (0 0 0 1) plane of Al_2O_3 indicated the (1 1 1)–(0 0 0 1) interface is more stable [39]. This orientation, preferred due to its low lattice misfit, has also been reported in other studies [14,38,40]. Our own matching tests confirmed that matching the Ni(1 1 1) plane with α-Al_2O_3(0 0 0 1) minimized the interfacial lattice misfit [1] to 3.3% compared to 10.4% and 6.9% misfit, respectively, for the Ni(100) and Ni(1 1 0) planes of comparably sized interface unit cells.

1.3. Experimental characterization of the Al_2O_3/Ni interface

Most experimental investigations of the clean Ni/alumina interface have concentrated on growing thin nickel films on an alumina substrate. Such studies are primarily designed to characterize the classic "metal-support" interactions of heterogeneous catalysis, specifically for Ni catalysts on alumina supports. Here, we study the inverse system, i.e. alumina on a nickel substrate, since the alumina "film" grows in on the bond coat alloy during thermal barrier coating oxidation.

A commonly used distinction between types of interfacial bonding is the division into two categories: physical and chemical interactions. These interactions for metal–alumina interfaces were discussed by Klomp [41], and later by Dalgleish et al. [15], who reported experimental works of adhesion for various transition metal–alumina interfaces in an article on the nature of metal–alumina interactions. The energetics of the physical interactions are described by the work of adhesion, given by the Dupré equation:

---

[1] We have previously defined [20,21] an order parameter μ that describes lattice misfit, $\mu = 1 - (2\Omega/(A_1 + A_2))$ where Ω is the overlap area and A_1 and A_2 are the surface areas of the metal and ceramic cells.

$$W_{ad} = \gamma_c + \gamma_m - \gamma_{cm} \tag{1}$$

with W_{ad} the work of adhesion, γ_c and γ_m the surface free energies of the ceramic and metal respectively, and γ_{cm} the interface free energy. W_{ad} can be measured experimentally via the contact angle, Θ, that a liquid drop of metal makes with the ceramic surface. The relationship, known as the Young–Dupré equation, in this case is

$$W_{ad} = \gamma_m(1 + \cos\Theta). \tag{2}$$

The W_{ad} reported for Ni on α-Al$_2$O$_3$ is 827 mJ/m^2 in H$_2$ at 1273 K using a modified sessile-drop method whereby TEM investigation of particle profiles is designed to study solid–solid metal–ceramic interfaces [14]. This study found the Ni to be nonwetting on the alumina substrate. The alumina surface in this study was primarily oriented along (0 0 0 1) planes, but other planes were present in smaller amounts. Although the metal was consistent in orienting a (1 1 1) plane parallel to the (0 0 0 1) alumina film, they did not observe preferential rotational orientations of the metal particles on the substrate. Another study, measuring solid–solid interface energies by particle profile investigations, determined a Ni/alumina work of adhesion of 670 mJ/m^2 in vacuum (480 and 340 mJ/m^2 in H$_2$ and He, respectively) at 1773 K [42]. In a more recent study, Venkataraman et al. [12] used continuous scratch tests to find the work of adhesion for a 1.0 μm nickel film on an alumina (1 1 $\bar{2}$ 0) substrate to be only 110 mJ/m^2 for a maximum substrate temperature of 348 K during deposition of the thin film. Clearly, the measured adhesion strengths are all quite weak, but they show a wide range of values, characteristic of the irreproducibility of such experiments due to the imperfect nature of the interface formed and the range of methods used to assess adhesion. In the current study, we examine ideal, well-characterized interfaces to predict the intrinsic adhesion strength.

Local bonding and chemistry at internal interfaces of several metal–alumina systems have been characterized by spatially resolved electron-energy-loss spectroscopy and high resolution electron microscopy [43,44]. Experimental evidence from studies of Ni/alumina cermets and Ni deposited on clean alumina in UHV shows the Ni/alumina interface forms direct Ni–Al bonds under reducing conditions at high temperatures [43,45]. The nickel–aluminum bonds were expected to form in tetrahedral units from EELS and HREM analysis of Ni/alumina cermets [43]. However, the interfacial ceramic termination may be sensitive to the specific metal and sample preparation technique; for instance, diffusion-bonded interfaces (where the metal–ceramic couple is formed via thermocompression of the two crystals, as in the work of Wan and Dupeux [40]) can differ from those produced by molecular beam epitaxy.

In 1990, Zhong and Ohuchi found that Ni deposited on a clean α-Al$_2$O$_3$(0 0 0 1) substrate in ultrahigh vacuum at room temperature showed no sign of reaction in XPS core level and valence band spectra [45]; similar results using diffusion bonding techniques had been previously reported [46]. At 1073 K in UHV, alumina was partially reduced by Ni deposition [45]. In the presence of oxygen, a spinel phase, NiAl$_2$O$_4$, is formed at high temperature (1073 K). The effect of this spinel phase on metal–ceramic interface adhesion is not entirely clear. It may introduce additional stress to the system [45], yet some experimental evidence indicates that the spinel phase could actually improve adhesion [47].

1.4. Previous theory investigating the metal–Al$_2$O$_3$ interface

A variety of previous theoretical studies have been designed to investigate metal–ceramic interactions. An exhaustive review of all such work is not possible here. Some of these studies are reviewed in articles by Finnis [48,49], Ernst [50] and by us [20]. Previous theory investigating "macroscopic" phenomena of Al$_2$O$_3$/Ni interfaces has studied the role of aperiodic interfacial void formations leading to spallation [51] and modeled the evolution of stress–strain hysteresis and cyclic plasticity [52]. Here, we will discuss only a small subset of the theoretical work that has been performed to investigate the microscopic nature of metal–ceramic systems; specifically we look at several studies related to metal–alumina interactions.

An early study by Johnson and Pepper [53] modeled Fe, Ni, Cu, and Ag atoms in contact with an alumina surface via self-consistent field Xα scattered-wave calculations on clusters. These calculations showed a chemical bond to be established between the *d* electrons of the metal and the ''nonbonding'' 2*p* electrons of oxygen anions on the alumina surface. They concluded that the bonding was primarily covalent, with decreasing strength across the series Fe, Ni, Cu, and Ag.

Three years after the Johnson and Pepper paper, several other reports were published relating to the Ni/Al$_2$O$_3$ interface. Andersen et al. used extended Hückel tight-binding (atom superposition and electron delocalization molecular orbital theory) cluster models to study the bonding of α-Al$_2$O$_3$ with Ni, Al and Y ''surfaces'' and to look at cation vacancy diffusion. The alumina cluster was similar to that used in the Johnson and Pepper study, but it was found that a 10-atom Ni cluster was much more weakly bound than the single Ni atom had been [54]. To study the Ni/alumina interface, Zdetsis and Kunz performed unrestricted Hartree–Fock calculations on a cluster embedded in a large, self-consistently determined point charge array. Using only one explicit Ni atom in their Ni/alumina ''interface'' calculations, they found an average interface bond strength of 5.3 eV and charge transfer of 1.5 e$^-$ from the Ni to antibonding states of the alumina surface [55]. Raatz and Salahub performed local spin density scattered-wave calculations on clusters designed to simulate a Ni cluster on a γ-alumina supporting medium [56]. The structural model for the γ-alumina support consisted of Al$_5$O$_8$ or Al$_5$O$_8$(H) clusters with Al–O bond distances set to 1.97 Å, the observed bond length in γ-alumina [57]. The theoretical approach in this study was comparable to the earlier Johnson and Pepper study except that a more accurate electron exchange-correlation potential was used. They found that the alumina support served to decrease the Ni magnetic moments and reported strong hybridization of the Ni-3*d* O-2*p* levels. Most of their paper was then devoted to exploring the effect that this had on subsequent chemisorption of CO.

A more recent DFT study modeled a similar Nion-alumina support and CO chemisorption scenario [58]. Linear combination of Gaussian-type orbital density functional calculations using the Xα approximation to the exchange-correlation potential were employed. The results of this study indicated a very large, 8.1 eV, adsorption energy resulting from a strong ionic bond formed between a single Ni atom and the oxygen from the alumina cluster. For a Ni cluster of six atoms, that adsorption energy decreased to 3 eV per atom due to Ni–Ni bonding.

In addition to Ni/Al$_2$O$_3$ studies, several DFT studies have been reported on the Nb/Al$_2$O$_3$-(0 0 0 1) interface [59–61]. Likewise, density functional studies of Al$_2$O$_3$ with Pt and Ag adsorption [62] as well as thin Al$_2$O$_3$ films on Al(1 1 1), Ru(0 0 0 1), and Mo(1 1 0) substrates with subsequent Pt (and a variety of other metals [63]) adsorption [64–66] have been investigated. Jennison et al. found that, for such metal substrates, thin alumina films (2–3 layers of oxygen) may prefer a structure that does not correspond to a conventional phase of alumina. Specifically, these films have Al ions occupying distorted tetrahedral positions (or a mix of tetrahedral and octahedral positions similar to κ-Al$_2$O$_3$ as found with a larger periodic unit cell) and have chemisorbed oxygen at the interface [64,66]. Although they did not specifically calculate any interfaces with Ni or nickel–aluminum alloys, they anticipated their results for alumina on aluminum would apply to NiAl-type substrates since they expect no Ni to be incorporated into the alumina film or to be in contact with the oxygen [64]; and they found local density approximation (LDA) binding of a Pd overlayer on the alumina/Al(1 1 1) to be similar to an experimental estimate for such a film on NiAl(1 1 0) [66]. By contrast to the suggestion that multiple layers of aluminum metal may reside at the alumina/NiAl interface, Lozovoi et al.'s DFT simulation of NiAl oxidation shows an Ni-rich surface at the interface with aluminum oxide to be energetically the most favorable interface of the possibilities they investigated [67].

Previous ab initio work investigating Ni/alumina has been limited to small clusters of alumina with one or more Ni atoms [53–56]. As seen in these previous works, the Ni–alumina bonding strength going from a single Ni atom on alumina

to a Ni cluster on alumina shows a marked decrease. It seems reasonable to expect that this trend of decreasing Ni–alumina interactions with increasing Ni cluster size would hold true – and be most pronounced – in the case of an ''infinite'' interfacial plane. Our approach represents such an Al_2O_3/Ni interfacial plane, as a result of the periodic boundary conditions. In contrast to previous studies, we chose to model a nickel substrate with increasing alumina ''coverage'', designed to model the growth of the TGO layer on the bond coat substrate in TBC's; to our knowledge, such a model has never before been studied. Furthermore, our calculations include full relaxation of the surfaces and interfaces of $Al_2O_3(0\,0\,0\,1)$ that, as we show later, has a large impact on surface and interface structure and energetics.

2. Computational methods

We performed first-principles spin-polarized DFT [68,69] calculations using the Vienna Ab Initio Simulation Package (VASP) [70–72]. These calculations employed periodic boundary conditions, expanded the valence electron density in a plane-wave basis, and replaced the core electrons with ultrasoft pseudopotentials [73,74]. Nonlinear partial core corrections to exchange and correlation were included for Ni and Al. For purposes of comparison, we performed both LDA and generalized gradient approximation (GGA) calculations for bulk and $(0\,0\,0\,1)$ surface α-Al_2O_3 calculations. The interface calculations were all performed using the GGA (PW91) [75,76]. Dipole corrections perpendicular to the interface were calculated for all surface and interface structures. To compare differences in interface adhesion between the LDA and GGA, we also calculated adhesion energies within the LDA for our most energetically favorable interface structures. The lattice vectors used for these calculations were the same as those used in all interface calculations, but the ionic coordinates were optimized within the LDA using the lowest-energy GGA ionic coordinates as the initial configuration.

The pseudopotential used in this study are those contained in the VASP version 4.4 database. These

nonlocal pseudopotentials are of the separable Kleinman–Bylander [77] form generated using the RRKJ scheme [78]. The local portion of the pseudopotential is the all-electron potential that has been unscreened with respect to the valence electrons beyond a given radius and smoothly matched at this radius to a zeroth-order Bessel function except in the case of Al, where the local part corresponds to the d pseudopotential. The database contains similar sets, i.e., both sets use the same parameters described below, that employ either the LSDA of Perdew–Zunger [79] or the GGA (PW91) [75,76] parameterization of the exchange-correlation functional.

The employed pseudopotentials were generated in the neutral $4s^13d^9$, $3s^23p^1$, and $2s^22p^4$ configurations for Ni, Al and O, respectively. The local component of the Ni pseudopotential had a pseudization radius of 0.88 Å. The ultrasoft Ni pseudopotential was augmented with two projectors for the s, p, and d channels. The s part had both inner (for the norm-conserving part of the augmentation functions) and outer cutoff radii set to 1.14 Å. The p and d channels for Ni had inner radii of 1.14 and 1.04 Å, respectively, and both p and d had outer pseudization radii of 1.29 Å. The Al pseudopotential had two projectors for the s and p but only one for the d. The Al local component corresponded to the norm-conserving d pseudopotential with a cutoff radius of 1.40 Å. The ultrasoft Al s and p channels had inner cutoff radii of 1.25 Å and outer pseudization radii of 1.40 Å. The O pseudopotential was augmented with two s and two p projectors with the local part having a radius of 0.54 Å. The O ultrasoft s channels had inner radii of 0.66 Å and cutoff radii of 0.80 Å; the p channels had corresponding radii of 0.82 and 1.01 Å, respectively. Partial core corrections were included for Ni and Al using truncation radii of 0.51 Å for Ni and 0.89 Å for Al.

The calculations consisted of three primary steps: bulk alumina and nickel calculations, alumina$(0\,0\,0\,1)$ and Ni$(1\,1\,1)$ surface calculations, and alumina$(0\,0\,0\,1)$/Ni$(1\,1\,1)$ interface calculations. For the bulk calculations, we tested for convergence of the **k**-point sampling density and kinetic energy cutoff, and relaxed the atomic and cell coordinates. We initially relaxed the surface

and interface structures with a 40% lower kinetic energy cutoff for the planewave basis. Once we obtained the optimized ionic coordinates with this smaller basis, we further relaxed the ionic coordinates with the converged planewave basis. This allowed faster convergence of the structures, and several test cases showed this did not affect the final geometries. For the surface calculations, we converged the energies with respect to slab and vacuum thickness and atomic relaxations.

The alumina(0 0 0 1) surface presents several cleavage plane options. In our calculations, we imposed the constraint of having stoichiometric alumina slabs with equivalent faces. This allowed two possibilities: a single Al layer termination, or an O layer termination with half of the O atoms removed on either side. Fig. 2 shows the hexagonal Al_2O_3 cell with an Al-terminated (0 0 0 1) cut that can result in surface slabs that maintain the Al_2O_3 stoichiometry and present equivalent alumina surfaces on each side.

In contrast to the Al_2O_3(0 0 0 1) surface, the Ni(1 1 1) surface presents a unique cleavage plane. Since we are modeling alumina growth on a nickel surface, we chose to impose the equilibrium bulk Ni lattice constants on our interface unit cells. In the ionic relaxation steps, the coordinates of the nickel atoms in the bottom layer of the nickel slab were initially fixed to bulk values. In the final relaxation steps, this restriction was lifted, although the resulting ionic relaxations in this nickel layer were very minor. As mentioned previously, the interface lattice mismatch between the Ni(1 1 1) and Al_2O_3(0 0 0 1) in our calculations was low, at only 3% for a hexagonal cell with a surface area of 21.4 Å^2. We initially calculated two different translational orientations of the alumina surface at the interface for each alumina thickness. The first was simply the interface formed by matching the (0 0 0 1) alumina plane (in-plane lattice vectors [0 1 0] and [$\bar{1}$ 0 0]) with Ni(1 1 1) (in-plane lattice vectors [0 1 $\bar{1}$] and [1 $\bar{1}$ 0]); the second, more energetically favorable translation was achieved by uniformly translating (in the xy plane) the alumina film in this original structure -1.2 Å parallel to the interface. This resulted in structures where a Ni atom occupied the position that the next Al layer would have occupied in the bulk alumina structure. The two translations corresponded to initial positioning of the interfacial Al ions above an hcp hollow site in one translation and an fcc hollow in the second translation. An energetically unfavorable starting configuration, where the interfacial aluminum was positioned directly over an interfacial nickel site, was also investigated for each of the three thicknesses of alumina; however, these relaxed to the same structures as those obtained with the energetically favorable fcc hollow translation described earlier. To further test whether our relaxed structures were trapped in local minima, the more energetically favorable (fcc hollow) translation relaxed structures were annealed, using Nosé's algorithm for constant temperature DFT–MD [80,81], for 0.4–0.7 ps at 1300 K using a time step of 40.0 fs and a Nosé frequency of 11.0 THz. The annealed structures were then quenched using the conjugate-gradient algorithm also employed in the relaxations of the initial structures previously described.

Providing a good means for setting the partial band occupancies for the metal is important for obtaining accurate descriptions of the total energy.
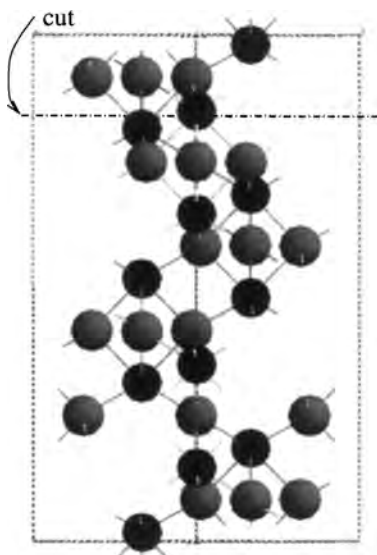

Fig. 2. Hexagonal unit cell of α-alumina showing preferred basal plane cut in between the two Al atoms. The black spheres represent aluminum atoms and the gray ones oxygen atoms.

We used two methods in our calculations. The first of these is the tetrahedron method with corrections introduced by Blöchl et al. [82]. The second method employed in our calculations was first-order Methfessel-Paxton smearing [83]. For these calculations, we chose a smearing width of 0.1 eV, which resulted in very small entropy terms (<0.5 meV/atom). Both methods gave the same total energies to within less than 0.5 meV/atom for our calculations.

For analysis of local charge densities, projection spheres around each atom must be defined. We defined spheres with radii of 1.015, 1.345, and 1.23 Å for Al, O, and Ni, respectively. These spheres have no impact on the total energy or density convergence in the calculation but merely determine the amount of charge density enclosed within the predetermined sphere around each atom for analysis purposes. The Al and O radii were chosen to capture most of the cell volume of bulk alumina with minimal overlap; these radii described a crystal of ~80% ionic character for the "bulk structure" expanded by 3% to fit the nickel substrate. Estimates ranging from ~60% to ~90% ionic character have been reported previously [84–87]. The sphere radii for Al and O were able to capture most of the electron density; however, the Ni radius resulted in ~1.25 e$^-$/atom in the interstitial regions. This value was maintained to minimize sphere overlap in our analysis of charge differences between atoms in the isolated slabs and the interfacial structures. Given the partial occupancy of the Ni 4s band, which is expected to be delocalized as it is in all metals, it is not surprising to find a large amount of the electron density in the interstitial regions.

3. Results and discussion

3.1. Bulk Al_2O_3 and Ni

We tested for convergence with respect to **k**-point sampling density, plane-wave basis, and equilibrium lattice volume, for bulk Ni and Al_2O_3. The most stringent of these converged values for energy cutoff and **k**-point sampling density in the two

bulk cases were then used for the surface and interface calculations. For the Ni bulk primitive cell calculations, we found a Monkhorst–Pack grid of $10 \times 10 \times 10$ **k**-points to be sufficient. As expected, the Al_2O_3 calculations were converged with a much lower **k**-point sampling of $3 \times 3 \times 3$ **k**-points for the primitive cell ($3 \times 3 \times 1$ for the hexagonal cell). A kinetic energy cutoff of 340 eV resulted in absolute energy convergence of at least 0.01 eV for our calculations; the use of ultrasoft pseudopotentials permitted converged energy values with this relatively small basis (in fact, Ni was well converged with a lower cutoff of ~300 eV). The kinetic energy cutoff for the augmentation charge grid was chosen to be 560 eV. This value had been previously tested for adequacy with the O pseudopotential employed and was higher than that required by the Al and Ni pseudopotentials [70–72]; our tests using a significantly higher cutoff (800 eV) for the augmentation charge basis showed that the lower value (560 eV) was indeed converged. The bulk structures were then optimized, by nonlinear fit to an equation of state, using the converged **k**-point and energy cutoff values. This was accomplished by performing single point calculations where we uniformly scaled the lattice vectors of the primitive cells for Ni and Al_2O_3 to sample the region within ~5% of the equilibrium value. The Ni volume within DFT–GGA was within 1% of experiment. An earlier study by Kresse et al. reported a bulk modulus [88], obtained using the Ni ultrasoft pseudopotential in VASP, that was within 5% of the experimental value [89]. For our alumina calculations, a nonlinear fit to Murnaghan's equation of state [90]

$$E(V) = \frac{B_0 V}{B_0'} \left[\frac{(V_0/V)^{B_0'}}{B_0' - 1} + 1 \right] + C \qquad (3)$$

(with $E(V)$ the total energy, V the volume, V_0 the equilibrium volume, B_0 the bulk modulus with pressure derivative B_0', and C a constant) showed that both LDA and GGA results had bulk moduli with <10% deviation from experiment and equilibrium volumes within 3% of the experimentally determined value [91].

Table 1

Comparison of LDA and GGA unrelaxed, E_{unrel}, and relaxed, E_{rel}, surface energies (mJ/m^2) and vertical relaxation (Δz in Å) of surface Al (inward) for three-, four-, and five-layer alumina slabs. Overbinding of LDA results in higher surface energies for those structures. Convergence of surface energy and structural relaxation is fairly good by the four-layer structure for both LDA and GGA calculations

α-Al$_2$O$_3$(0 0 0 1)	LDA			GGA		
	E_{unrel}	E_{rel}	Δz	E_{unrel}	E_{rel}	Δz
Three layer	4016	1866	0.81	3509	1401	0.84
Four layer	4014	1961	0.73	3509	1496	0.74
Five layer	4006	1957	0.71	3505	1494	0.73

3.2. Al$_2$O$_3$(0 0 0 1) and Ni(1 1 1) surfaces

The *x*, *y*, and *z* coordinates of all atoms in the surface calculations were free to relax within the fixed lattice vectors determined from equilibrium bulk calculations and with inclusion of at least 10 Å vacuum. Such a model produces two free surfaces, hence the surface energy is calculated by subtracting the surface cell energy from the bulk energy (for the same number of atoms) and normalizing by twice the area of the *xy* plane of the surface cell. We calculated the relaxed surface energy for Ni(1 1 1) for 3–5 layer slabs and found the surface energy of Ni(1 1 1) to be converged within 2% of the five-layer value for even the three-layer case. For our alumina surface calculations, we investigated both aluminum and oxygen-terminated surfaces. After some preliminary calculations with the O-terminated surface, we determined this surface to be much less energetically favorable (2920 mJ/m^2 for a five-layer slab compared to 1490 mJ/m^2 for a five-layer [2] Al-terminated slab within DFT–GGA(PW91) calculations) and focused on the stoichiometric, Al-terminated cuts for all subsequent surface and interface calculations. Our findings of the Al-terminated Al$_2$O$_3$(0 0 0 1) surface as the most stable is consistent with similar predictions from DFT embedded cluster calculations [92]. The alumina(0 0 0 1) relaxed surface energies were well converged for four- and five-layer slabs. For three-, four-, and five-layer alumina slabs, we found fairly similar (large) inward

relaxation of the outermost Al atoms, which resulted in a very large energy lowering compared to the unrelaxed (bulk-terminated) surfaces. The surface energies and vertical inward relaxation of the surface aluminum for Al$_2$O$_3$(0 0 0 1) three-, four-, and five-layer slabs are shown in Table 1. In Table 2 we compare our LDA and GGA five-layer slab surface energy predictions with several previously predicted Al$_2$O$_3$(0 0 0 1) surface energy values for slabs with atomic coordinates both unrelaxed

Table 2

Comparison of predicted energies (mJ/m^2) for unrelaxed and relaxed surfaces for the basal plane of α-Al$_2$O$_3$ (reported energies rounded to three significant figures for consistency)

	Unrelaxed	Relaxed
Empirical potentials		
Electrostatic and shell model[a]	6530	2970
Two and three-body potentials[b]	5040	2040
Two body and shell model[c]	5950	2030
First principles		
HF/four layer[d]	5320	3920
LDA/three layer[e]	3770	1760
LDA/five layer[f]	4010	1960
GGA/five layer[g]	3510	1490
Experimental:	~925[h]	

[a] Tasker [95] using empirical electrostatic shell-model potentials [116,117].

[b] Blonski and Garofalini [96] using a two- and three-body empirical potential.

[c] Mackrodt et al. [36] using an empirical two-body potential [118] and the same shell-model employed in Ref. [95] for electron polarization.

[d] Causá et al. [94], four-layer slab using 2D periodic Hartree–Fock calculations.

[e] Manassidis et al. [34,35] using LDA for a three-layer slab.

[f] This paper: LDA, five-layer slab.

[g] This paper: GGA, five-layer slab.

[h] Experimental value extrapolated to 0 K.

---

[2] By "layer" we mean an Al$_2$O$_3$ unit that consists of a plane with three oxygen atoms and an aluminum on either side of that plane, i.e. Al–O$_3$–Al. Six such layers make up the hexagonal unit cell of α-Al$_2$O$_3$.

and relaxed. Although there is considerable variation in predicted surface energies, the importance of allowing atomic relaxations is evident in each study. A recent DFT study by Wander et al. found that the specific choice of exchange-correlation functional has some effect on the predicted surface structure [93]. Since alumina is a highly ionic material, the bulk-like surface termination is unfavorable since it leaves "bare" surface $Al^{\sim 3+}$ ions; thus a large inward relaxation of surface aluminum cations results in a more energetically favorable structure whereby the oxygen anions can screen more effectively the positive charge of the aluminum ions. We found large inward relaxation of the surface aluminum ions in all cases, as has been reported previously [34–36,94–96]. The Al–O bond length from bulk calculations using GGA was 1.87 Å; this decreased to 1.67 Å for the surface Al–O bonds upon relaxation. The decrease in bond length was associated with a 0.73 Å vertical relaxation of the surface aluminum (on each side of the slab), concurrent with horizontal expansion of the hexagonally packed oxygen atoms in the outermost oxygen planes. Previous studies that allowed only relaxation of the interlayer spacing could not include this effect [34,35,59]. More recent studies investigating $Al_2O_3(0\,0\,0\,1)$, using Hartree–Fock and LDA calculations, have reported geometrical relaxations for 9- and 18-layer slabs but did not calculate surface energies [62,97]. LDA calculations by Verdozzi et al., for a surface with 18 layers, showed comparable vertical relaxations to our calculations for the outermost layers. Both calculations showed inward vertical relaxations for the surface aluminum of 0.73 Å, an outward expansion of the terminating oxygen plane of 0.03 Å, and the subsequent Al–Al layers showing a vertical distance decreased by 0.21 Å, compared to 0.22 Å in our five-layer GGA case [62].

Experimental characterization of the energetics and surface structure of $(0\,0\,0\,1)$ plane of α-Al_2O_3 is somewhat complicated. In fact, the surface structure of α-$Al_2O_3(0\,0\,0\,1)$ is sufficiently complicated and conditions dependent to warrant its inclusion in a 1997 article by Chame et al. entitled "Three mysteries of surface science" [98]. Obtaining the ideal cleavage plane (the Al-terminated surface studied theoretically) by fracture studies

using the double-cantilever-cleavage technique is difficult or impossible [37]. However, as mentioned earlier, the $(0\,0\,0\,1)$ surface can grow in during Al_2O_3 formation via aluminum oxidation [33] and calculations have shown the ideal single-Al terminated surface to be one of the lowest energy surfaces of α-Al_2O_3. Below $\sim$1220 K, it is difficult to obtain reliable surface energies of clean Al_2O_3 due to hydroxylation. An expression for the experimental surface energy of the alumina $(0\,0\,0\,1)$ surface is 892(ergs/cm^2) – 0.12 T(°C) obtained by measures at 1363°C and 4660°C and assuming a constant coefficient in the temperature range [99]. As we mentioned in a previous article [23], the reliability of such an estimate over the temperature range is not possible to ascertain with only two data points, and its validity in extrapolation to much lower temperatures might also be suspect. Nevertheless, assuming that a constant coefficient is a reasonable approximation, the experimental estimate of 925 mJ/m^2 for the $(0\,0\,0\,1)$ plane of α-Al_2O_3 at 0 K is well below any of the theoretically predicted values shown in Table 2, although our DFT–GGA predicted surface energy is closest to this value.

As expected, the nickel surfaces showed very little atomic relaxation. We obtained a GGA surface energy of 1950 mJ/m^2 for the five-layer Ni(1 1 1) surface, compared with 2011 mJ/m^2 for previous full charge density linear muffin-tin orbital calculations [100] (an all-electron density functional-based GGA calculation) and experimentally determined values of 2380 [101] and 2450 mJ/m^2 [102]. Our calculations showing that Ni(1 1 1) has a higher surface energy than Al_2O_3-$(0\,0\,0\,1)$ are consistent with the experimentally observed nonwetting of Ni on alumina [42], assuming no significant interfacial chemical reaction takes place (which seems reasonable, since no reaction was observed, based on both core and valence band photoemission spectra during Ni deposition at room temperature) [45]. The relatively high surface energy of Ni(1 1 1) means that Ni will prefer to aggregate to minimize the amount of surface exposed, whereas the somewhat lower (based on our calculations) surface energy of alumina's basal plane suggests that Al_2O_3 will favor allowing exposed surfaces.

3.3. The Al₂O₃(0 0 0 1)/Ni(1 1 1) interface

From our previous explanation of the non-wetting of Ni on alumina, it seems reasonable to expect that coating would occur in the reverse system, alumina on Ni, since Al_2O_3's surface energy is less than that of Ni. We do find that Al_2O_3 can coat Ni; nevertheless, we observe weak adhesion for the alumina/Ni interface. Before embarking on the interface studies, a rigorous check of the adequacy of our planewave basis was made. We performed one calculation of a Ni(1 1 1) surface with one layer of Al_2O_3(0 0 0 1) at a energy cutoff of 600 eV for the planewave basis and 800 eV for the augmentation charge. We found the total energy of this system was converged within 0.7×10^{-4} eV to that of our lower energy cutoff, where we were converging within a tolerance of 0.1×10^{-4} eV, which assured us of the adequacy of our basis. Uniformly expanding the bulk alumina crystal to match the Ni(1 1 1) lattice vectors results in a energy increase of 0.16 eV per bulk Al_2O_3 unit, or 0.03 eV/atom. Accordingly, all interface adhesion energies are calculated by subtracting the energy of the infinitely separated nickel slab and the expanded alumina slab from the total energy of the interface cell calculation. In other words, the adhesion energy is defined as the energy lowering achieved by interface formation compared to the energies of the two isolated slabs.

We calculated structures corresponding to two different translations of the α-alumina layer on the Ni substrate. We found that the interface structures relaxed to distinct structural local minima. The translation corresponding to initial aluminum positioning over fcc hollow sites of the Ni(1 1 1) surface resulted in the energetically more favorable relaxed structures. The initially hcp hollow site positioning produced somewhat higher energy (local minima) structures for the three cases. The calculated works of adhesion for the translations differed by 10% for one layer of alumina, 18% for two alumina layers, and 29% for three alumina layers. This increasing discrepancy with increasing number of layers seemed related to the increasing "stability" of the α-alumina structure, i.e., the three-layer alumina geometry was less able to rearrange for optimal substrate bonding due to more favorable intra-ceramic bonding. Our most energetically stable interfaces corresponded to translation of the alumina such that the starting configuration had a Ni atom occupying the space where the next Al layer would have been in bulk alumina, with the surface aluminum positioned over an fcc hollow site as described earlier. From this initial point, we found that the work of adhesion first increased with layer thickness, then decreased: 618 mJ/m² for one layer of Al_2O_3 on Ni, 943 mJ/m² for two layers of Al_2O_3 on Ni, followed by a decrease to 456 mJ/m² for the three-layer case.

Calculations using the LDA to DFT resulted in similar trends in adhesion energies. The adhesion energies calculated within the LDA were larger than those obtained from the GGA calculations, which is to be expected since LDA is notorious for overbinding. Within the LDA, using the GGA lattice vectors but LDA-relaxed ionic coordinates, the monolayer of Al_2O_3 on Ni had an adhesion energy of 1255 mJ/m², two layers of Al_2O_3 on Ni resulted in a 1506 mJ/m² adhesion energy, and the adhesion energy of three layers of Al_2O_3 on Ni decreased to 858 mJ/m². To test that the slight expansion (<2%) of the GGA Ni lattice vectors over the ideal LDA ones was not a significant factor in this increased adhesion, calculations using the ideal LDA lattice vectors were also performed. These yielded similar (within ~10%) adhesion energies to those obtained with the GGA lattice vectors. Although it is expected that the LDA results overestimate the adhesion energies, it is possible that the GGA overcorrects for the LDA overbinding and provides a low estimate. The GGA weakening of adhesion relative to LDA for metal adsorption on alumina was reported by Bogicevic and Jennison in their study of various metal adsorptions on ultrathin alumina films [63].

Cross-sectional views of the relaxed structures of one, two, and three layers of alumina on Ni can be seen in Figs. 3 (the most energetically favorable) and 4 (a higher energy, local minimum structure). Top views of the interfacial Al_2O_3 layer on the interfacial Ni layer for both translations of the three different alumina film thicknesses are shown in Figs. 5 and 6. Annealing and quenching the more energetically favorable structures did not result in enhanced works of adhesion. The one-layer
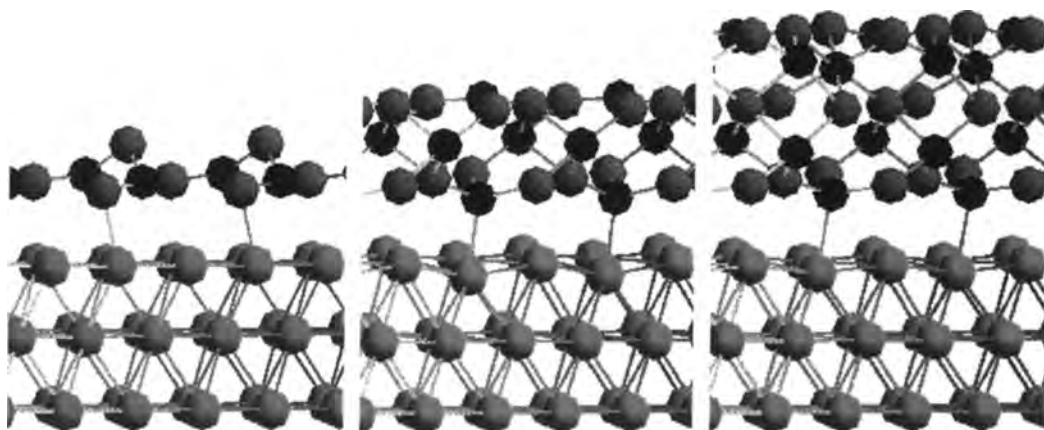
Fig. 3. One, two, and three layers of $Al_2O_3(0\,0\,0\,1)$ on $Ni(1\,1\,1)$ – most energetically favorable translation at the interface. The black spheres represent Al atoms and the dark gray ones are O atoms. The lower three planes of light gray spheres are Ni.
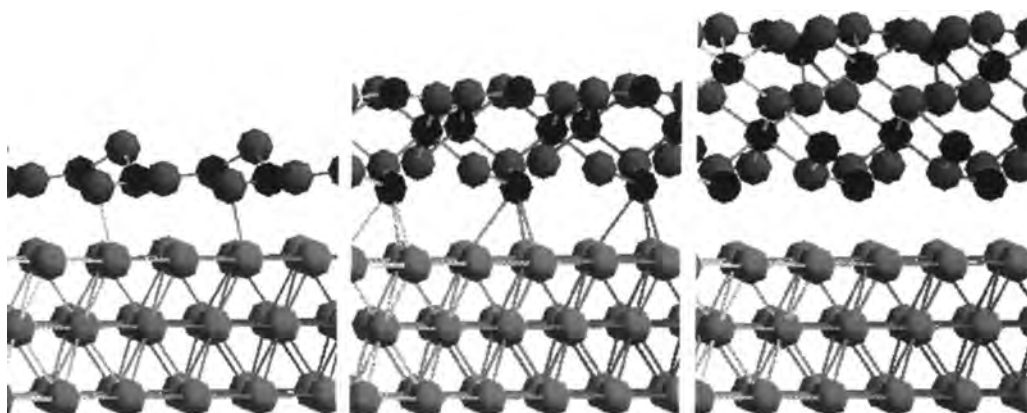

Fig. 4. One, two, and three layers of $Al_2O_3(0\,0\,0\,1)$ on $Ni(1\,1\,1)$ – less energetically favorable interfacial translation (local minimum). The black spheres represent Al atoms and the dark gray ones are O atoms. The lower three planes of light gray spheres are Ni.

annealed structure was energetically identical to the initial relaxed structure, and the two- and three-layer annealed structures actually resulted in structures analogous to the relaxed structures from the (less stable) hcp hollow site translation. Likewise, as previously mentioned, the energetically unfavorable starting configuration with the interfacial aluminum ions positioned directly on top of interfacial nickel ions relaxed to the same final structures as those obtained for the fcc hollow site translation.

A single layer of alumina transforms to an amorphous structure that breaks the planarity of

the oxygen layer upon relaxation; the two and three layer films of alumina basically maintain the oxygen planes as in bulk alumina. The nearest-neighbor distances across the interface for Ni–O and Ni_3–Al are shown in Table 3. The bond lengths shown in this table correspond to the nearest-neighbor distances between unique atomic sites shown in Figs. 5 and 6. For both translations, the two- and three-layer relaxed structures had Al atoms closest to the nickel surface, with a planar hexagonal array of O atoms above the interfacial Al atoms. The single-layer structures break the planarity of the oxygen layer, resulting in nearest
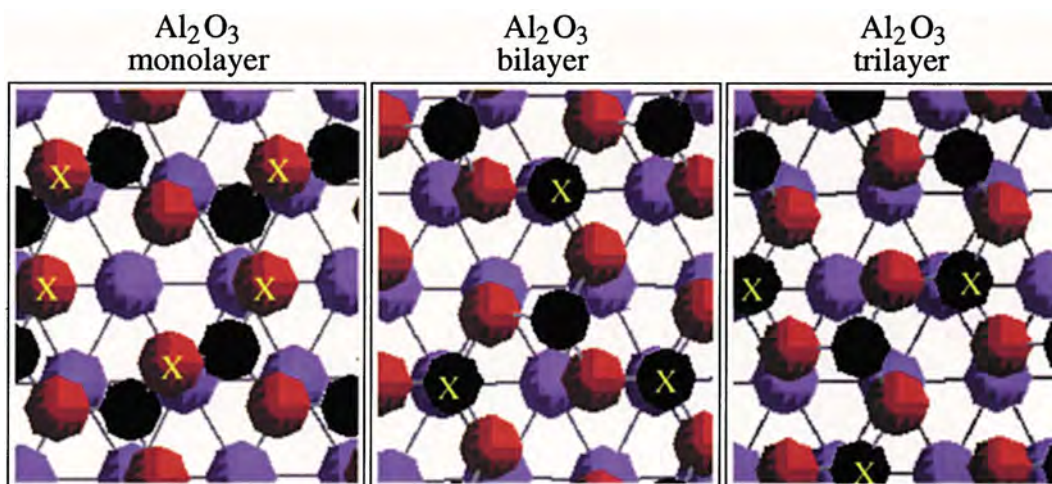
Fig. 5. Top view of the Al_2O_3 layer at the interface with Ni for one, two, and three layers of $Al_2O_3(0\,0\,0\,1)$ on $Ni(1\,1\,1)$ – most energetically favorable translation. The black spheres represent Al atoms, the red ones are O atoms, and the purple ones Ni atoms. The yellow "X"'s denote representative atoms nearest to the Ni.
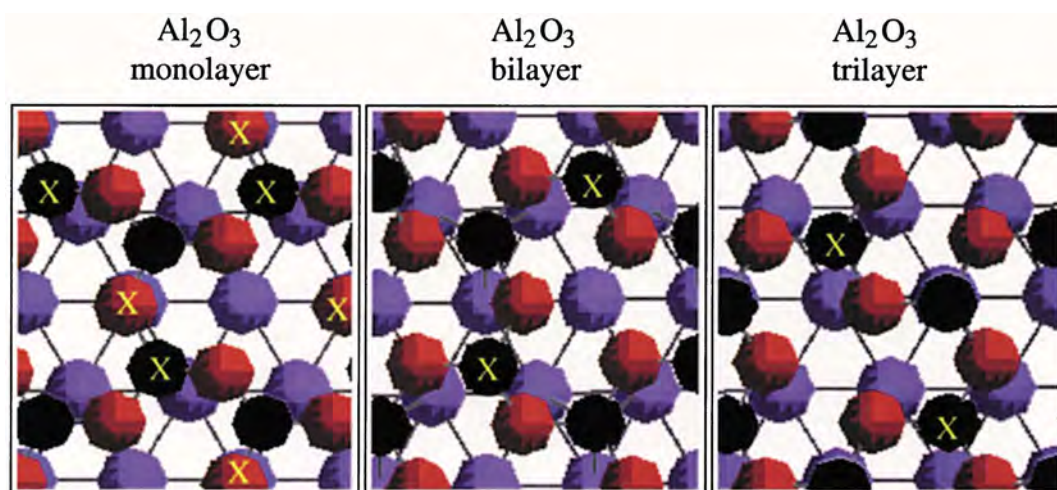

Fig. 6. Top view of the Al_2O_3 layer at the interface with Ni for one, two, and three layers of $Al_2O_3(0\,0\,0\,1)$ on $Ni(1\,1\,1)$ – less energetically favorable translation. The black spheres represent Al atoms, the red ones are O atoms, and the purple ones Ni atoms. The yellow "X"'s denote representative atoms nearest to the Ni.

approach of O atoms rather than Al, with the Al atoms somewhat farther from the interface in the "middle" of the alumina film; O atoms are also on the surface exposed to vacuum, i.e., farthest from the nickel surface. As can be seen from this table, the higher energy (local minimum) two- and three-layer Al_2O_3 structures resulted in Al–Ni bond

distances that roughly correspond to Ni_3–Al bonding, i.e. the relaxed Al at the interface occupied a position with nearly equal distances from the three Ni atoms at the interface (hcp hollow site), but did not have as close an approach for Ni–O. Experimental binding energies and relative composition ratios suggest Ni_3Al intermetallic interactions at

Table 3
Nearest-neighbor distances across the alumina/Ni interface for two translations of α-Al_2O_3(0 0 0 1) on Ni(1 1 1). See Figs. 3 and 4 to see the symmetry-broken monolayer film structure. Al_1 is the Al that is nearest to the nickel surface, Al_2 is the Al that is farther from the nickel surface in the Al_2O_3 monolayer

	Ni–O (Å)			Al to 3 nearest Ni (Å)
	O_1	O_2	O_3	
Lowest energy films				
One layer	2.16	2.17	3.39	Al_1 2.68, 2.73, 2.85
				Al_2 2.69, 2.75, 2.85
Two layer	2.34	2.46	2.58	2.25, 2.91, 3.02
Three layer	2.37	2.50	2.59	2.32, 2.98, 3.15
Higher energy films				
One layer	2.05	2.97	3.43	Al_1 2.67, 2.88, 3.13
				Al_2 2.91, 2.95, 3.29
Two layer	2.77	2.80	2.88	2.56, 2.58, 2.62
Three layer	2.70	2.71	2.76	2.63, 2.65, 2.70

the Ni/Al_2O_3 interface [45]. The binding energy and XPS line shapes also suggest perhaps NiAl interfacial interactions, but not Ni_2Al_3 or $NiAl_3$ [45,103]. The lower energy minima for the two- and three-layer structures resulted in a pronounced Ni–Al rather than Ni_3–Al arrangement, and achieved much shorter Ni–O distances. For comparison, the experimentally determined nearest-neighbor distances in the bulk cubic crystals of NiO (NaCl structure), NiAl (B2 structure), and Ni_3Al ($L1_2$ structure) are 2.09 Å [104], 2.50 Å, and 2.52 Å, respectively [105,106]. Thus, we see that none of the Ni–O bonds at the interface are as short as those in bulk NiO, whereas some of the Ni–Al bonds are even shorter than those in bulk NiAl and Ni_3Al. To the extent that bond length correlates with bond strength and given the weak adhesion, it appears that the long Ni–O interactions must play a significant role in the trends in adhesion. However, from our projected atomic charge density analysis presented later, it is clear that conventional ionic Ni–O bonds are not formed in these structures; rather, there is some energetic preference for "close contact" at the interface despite the lack of ionic bond formation across the interface. The preference for ionic bonding is effectively isolated to interactions between Al and O.

Fig. 7 displays the density of states (DOS) for the separated and combined interface systems. The absolute energies have been aligned according to the Fermi level (set to 0.0) for the Ni and interface DOS. Since the isolated alumina is insulating, we aligned the top of its O 2s band to the O 2s band of the interface DOS for purposes of comparison. The DOS of the interfacial system appears to be very nearly the sum of the two isolated systems. Analysis of charge densities projected onto atoms shows limited charge differences of the interfacial atoms from those of the isolated systems. Table 4 shows the difference between the isolated and combined systems' projected local charge densities for the Al_2O_3 interfacial layer and the Ni atoms at the interface. We did not observe charge donation, as reported in previous cluster studies [55], from the Ni to our stoichiometric alumina slab. The overall increase in charge for interfacial atoms was generally due to increased localization of the charge density in the interfacial region compared to the more diffuse free-surface density. The lack of new DOS features and charge transfer suggests, as reported from previous experimental observations [45,46], that low-temperature formation of α-Al_2O_3/Ni interfaces results in very limited or nonexistent interfacial reaction.

Figs. 8 and 9 display valence electron density plots for vertical cuts through one, two and three layers of Al_3O_3 on Ni. One of the more dramatic effects to be noted from these figures is the equivalent contour from the Ni reaching toward the interfacial aluminum, indicated by the red arrows, in Fig. 9. The presence of Ni–Al interactions is
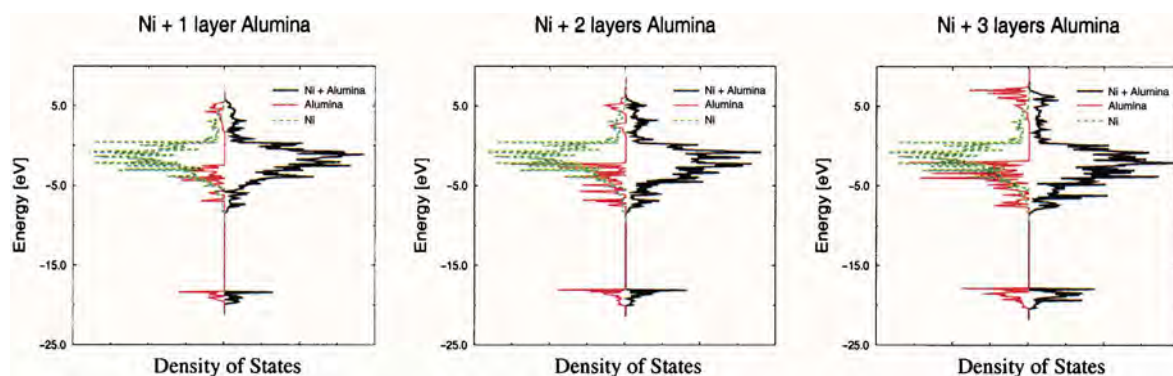
Fig. 7. DOS of isolated slabs, right, and interface systems, left, for one, two, and three layers of alumina on Ni(1 1 1).
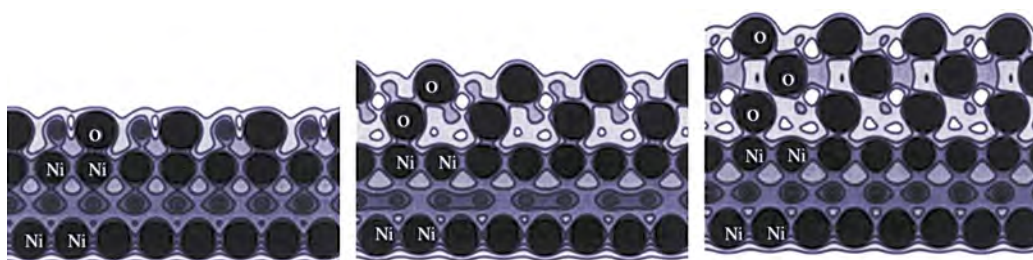

Fig. 8. Valence electron charge density cut near interfacial oxygen of one, two, and three layers of Al_2O_3 on Ni. There are 10 equivalent contours shown (spanning 0 to 1). The darkest regions correspond to the highest charge density values.
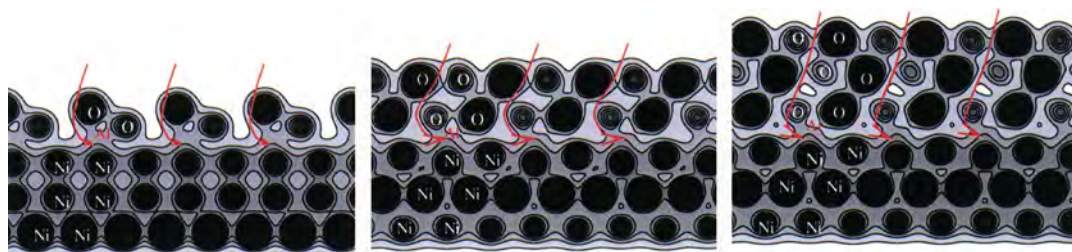

Fig. 9. Valence electron charge density cut near interfacial aluminum of one, two, and three layers of Al_2O_3 on Ni. There are 10 equivalent contours shown (spanning 0 to 1). The darkest regions correspond to the highest charge density values. The red arrows mark the density contour from the Ni reaching towards the Al at the interface. The Al itself is not apparent since it has very little associated valence electron density.

also apparent when analyzing the projected charge densities (Table 4). Also noteworthy are the decreasing equivalent contours enclosing Ni–O regions with increasing alumina film thickness in Fig. 8. This suggests decreasing Ni–O interactions as the alumina film thickens. The decreasing Ni–O interactions can also be seen from the charge

transfer for the interfacial atoms in Table 4. In Table 4, charge differences between the isolated slabs and the interfacial structure are apparent for NiAl (ascribed to the case where a single Ni–Al bond length is significantly shorter than the other Ni–Al bond lengths shown in Table 3) and Ni_3Al-like (ascribed to the situation where three Ni–Al

Table 4
Charge difference (e⁻/atom) projected onto the interfacial Al_2O_3 and Ni. The difference is taken between the projected interfacial atomic charges and those of the isolated systems with the same atomic positions. In nearly all cases shown, this difference is $\geqslant 0$. The atomic labels Al_1, Al_2, etc. are the same as those shown in Table 3. The Ni labels refer to the unique interfacial nickel positions, with the Ni_1 referring to the nickel with smallest nearest-neighbor aluminum distance. Ni_2 and Ni_3 are the interfacial nickel positions next nearest to the aluminum, i.e., making up the $\sim Ni_3Al$. Ni_4 is the fourth unique Ni position in the interfacial periodic unit and is farthest from the interfacial Al, i.e., does not participate in Ni–Al bonding

Atom	Lowest energy structure			Higher energy structure		
	1 layer	2 layer	3 layer	1 layer	2 layer	3 layer
Al_1	0.01	0.06	0.04	0.01	0.04	0.02
Al_2	0.01	–	–	0.00	–	–
O_1	0.07	0.05	0.03	0.10	0.01	0.00
O_2	0.07	0.03	0.02	0.01	0.00	0.00
O_3	0.03	0.04	0.02	0.00	0.00	0.00
Ni_1	0.09	0.15	0.13	0.07	0.05	0.04
Ni_2	0.05	0.00	0.00	0.04	0.05	0.04
Ni_3	0.04	0.00	0.00	0.04	0.04	0.03
Ni_4	0.00	0.00	0.00	0.00	−0.01	0.00

bond lengths shown in Table 3 are roughly equivalent to each other) interactions; the Al–Ni nearest neighbors in the lowest-energy structures each show relative electron density increase in the interfacial environment relative to the isolated surface electron density. Similarly, in the higher-energy structure, there is a charge increase for the interfacial Ni_3Al atoms relative to these atoms' isolated surface charges. Although the interfacial O atoms do show some charge increase, their nearest-neighbor Ni atoms show no corresponding increase or decrease for the lowest energy two- and three-layer structures. As can be seen from this table, the difference in atomic charges between isolated surface and interfacial environments was very minor in all cases. Since there is negligible Ni–O charge transfer, it seems plausible that the decreasing Ni–O charge density contours in Fig. 8 is related to the increasing stability of the alumina structure for increasing alumina film thickness.

Although these density plots are somewhat informative, perhaps a more useful tool for characterization of bonding is the electron localization function (ELF) [107,108]. This function is helpful in the classification of chemical bonding characteristics by analysis related to the Pauli exclusion principle. Mathematically, the ELF takes the form

$$\mathrm{ELF}(\mathbf{r}) = \frac{1}{1 + [D(\mathbf{r})/D_h(\mathbf{r})]^2} \qquad (4)$$

where $D(\mathbf{r})$ is the Pauli excess kinetic energy density [3] and $D_h(\mathbf{r})$ is the kinetic energy of the homogeneous electron gas for a density equal to the local density [109]. The ELF value is 0.5 for a homogeneous electron gas and can increase to ~ 1.0 for electrons paired in a covalent bond or a highly localized, unpaired electron in a dangling bond [110]. ELF values below 0.5 are less readily understandable. These can correspond to regions of very low electron density. Figs. 10 and 11 show cross-sectional ELF cuts of the Al_2O_3/Ni system for one, two, and three layers, for cutting near interfacial O atoms and Al atoms respectively. [4] Fig. 10 shows very little localization between the interfacial O ions and the Ni surface, especially for the two- and three-layer cases. In sharp contrast

---

[3] $D(\mathbf{r}) = T + T_{\mathrm{corr}} - T_{\mathrm{Bose}}$, where T is the kinetic energy of the noninteracting Kohn–Sham system ($-2\frac{\hbar^2}{2m}\sum_i \phi_i^* \nabla^2 \phi_i$), the kinetic energy "correlation" correction component is $T_{\mathrm{corr}} = (1/2)(\hbar^2/2m)\nabla^2 \rho$ to ensure $T + T_{\mathrm{corr}}$ is positive definite, and T_{Bose} is the ideal Bose gas kinetic energy ($(1/4)(\hbar^2/2m) \times (|\nabla\rho|^2/\rho)$).

[4] The low ELF values within the nickel slab arise from the delocalized, metallic electron density of the Ni. The ultrasoft pseudopotential augmentation density, which primarily affects the localized region around Ni nuclei as can be seen from the density plots, is not included, since this density is not contained in the Kohn–Sham orbitals. These plots display a qualitative picture of bonding between Ni–Al and show strong localization of valence electron density on oxygen anions as expected.
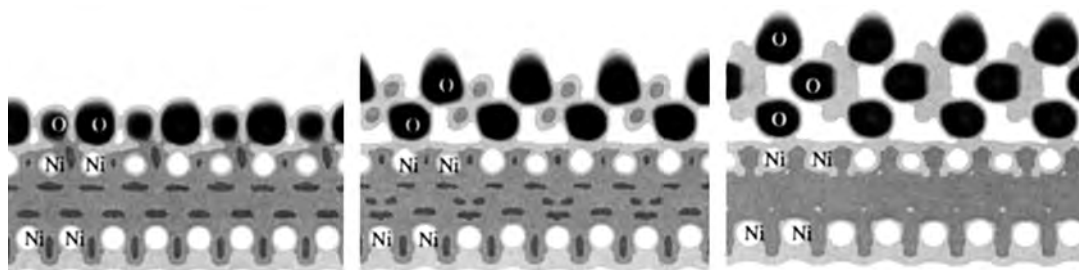
Fig. 10. ELF (of the ultrasoft pseudocharge density) cut near interfacial oxygen of one, two, and three layers of Al_2O_3 on Ni. There are eight equivalent contours to span a range from 0.0 to our highest value of $\sim$0.85 for these ELF cuts. The darkest regions are the region of highest ELF value.
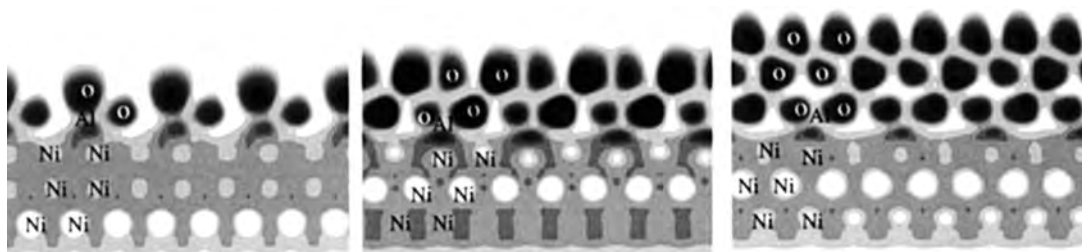

Fig. 11. ELF (of the ultrasoft pseudocharge density) cut near interfacial aluminum of one, two, and three layers of Al_2O_3 on Ni. There are eight equivalent contours to span a range from 0.0 to our highest value of $\sim$0.85 for these ELF cuts. The darkest regions are the regions of highest ELF value.

to Fig. 10, Fig. 11 shows a higher degree of localization between the interfacial Al and Ni, most notably for the two-layer case. It seems likely this electron localization between the Ni–Al is largely responsible for the high W_{ad} value for the two-layer case compared to the one and three layer W_{ad}'s.

3.4. Summary and implications for thermal barrier coatings

We have investigated the (0 0 0 1) surface of α-alumina and its interface with Ni(1 1 1). Consistent with the experimental observations of Zhong and Ohuchi [45], we find limited interaction between the surfaces at low temperature in vacuum. Charge transfer across the interface is negligible in our calculations, a markedly different prediction from those of previous Ni/alumina cluster

calculations [55,58]. As mentioned earlier, previous extended Hückel tight-binding cluster simulations showed a marked decrease in adhesion of Ni clusters, compared to that of Ni atom, on an alumina substrate [54]. This is consistent with the results of recent studies that have investigated increasing metal coverage from 1/3 ML to 1 ML of non-Ni metals on alumina where they find ionic bonds dominate at low metal coverage but that the attraction is a result of polarization at high metal coverage [63]. We find unexpected and unconventional changes in the interfacial structures and interactions going from one to three layers of alumina film thickness on Ni. We find that the Ni–O interactions are more pronounced in the monolayer structure, W_{ad} is strongest for the two-layer case due to localized Ni–Al interactions, while the three-layer structure exhibits much weaker Al_2O_3–Ni interactions at the interface, instead preferring intra-ceramic interactions.

These subtle and complex collective effects would likely prove difficult or impossible to model with simple analytic potentials. By looking at the related system of increasing alumina thickness on a nickel substrate and finding a dramatic decrease in adhesion for the thickest alumina coatings studied, our results complement the findings of the Ni cluster study and provide further insight into the nature of the interfacial interactions for Al_2O_3/ Ni. The weak adhesion for this interface is supportive of clean Al_2O_3/Ni displaying weak metal-catalyst support interactions. It is likely that any strong interactions that exist between the support and active phase are primarily due to intermediate oxide and aluminate formation, as indirectly suggested by de Korte et al. in their XRD and reduction behavior measurements of coprecipitated catalysts [111].

As mentioned earlier, the actual interface between the bond coat alloy and alumina in a TBC system might be highly complex. We believe the interface studied here to be a reasonable approximation to the interface resulting from TBC bond coat oxidation since excess oxygen is available to react with any aluminum that migrates to the ceramic–metal interface, and the percentage composition of aluminum in the bond coat is small. Although some progress has been made using DFT calculations to predict the oxidation of NiAl [67] and a nonstoichiometric description of the alumina might prove desirable [64], an exact description of interfaces in complex systems is still far from achievable with current computational size limitations. Nevertheless, we believe this in-depth investigation of an ideal Ni(1 1 1) interface with α-Al_2O_3 provides valuable insight into adhesion trends and bonding in this system.

Recent experiments have shown delamination between the bond coat alloy and alumina in failed TBC's as well as fracture between the zirconia top coat and alumina [112–114]. Our work provides new insight into the atomic-level cause for this bond coat-alumina delamination with increasing alumina thickness. Namely, the strain from thermal cycling and bond coat oxidation may readily permit delamination between the alumina and nickel due to the very weak interfacial adhesion.

Our previous characterization of the ZrO_2/Al_2O_3 interface led to the conclusion that this ceramic–ceramic interface is also weakly adhered [21]. Accordingly, limiting alumina formation may be a key factor in extending the operating lifetime of the TBC.

Excessive bond coat oxidation leading to thick alumina scale formation is detrimental to TBC performance lifetimes; finding means to limit this process should help to solve this problem. Discovering chemical means to protect the superalloy from oxidation by forming slow-growing oxides with favorable adhesion may be the critical aspect of materials technology that will allow further advances in TBC performance. Recent experimental work by Pint et al. investigated the effect of reactive elements such as Pt on alumina scale adhesion [30]. They found that, although Pt addition to a nickel aluminide bond coat did improve metal–ceramic adhesion, it was not as successful as certain other elements, i.e., Zr and Hf. Pint et al. speculate this was because it was not as effective in reducing the oxide scale growth rate or changing the α-Al_2O_3 crystal structure. Nevertheless, Pt addition to bond coatings in TBC's has become rather popular. Another study found that depositing a layer containing Pt between the zirconia top coat and the bond coat alloy improved oxidation resistance. They interpreted this improvement as due to Pt decomposition of alumina at high temperatures [115]. Of course, a natural approach to limiting alumina scale growth would be to limit the Al content, and hence Al_2O_3 formation, in the bond coat alloy itself. We are currently investigating candidate metals with which to replace some or all of the aluminum content in the boat coat. This may result in TBC's that can be fabricated with the same methods as those currently employed, but which will have longer performance lifetimes due to increased oxidation resistance and/or improved adhesion of the zirconia to the bond coat alloy.

Acknowledgements

References

[1] V. Gupta, A.S. Argon, J.A. Cornie, D.M. Parks, Mater. Sci. Engng. A 126 (1990) 105.

[2] V. Gupta, A.S. Argon, D.M. Parks, J.A. Cornie, J. Mech. Phys. Solids 40 (1992) 141.

[3] G.L. Nutt, W.E. King, in: D.B. Miracle, D.L. Anton, J.A. Graves (Eds.), Intermetallic Matrix Composites II Symposium, Pittsburgh, Mater. Res. Soc. 1992, pp. 331–336.

[4] A.G. Youtsos, M. Kiriakopoulos, T. Timke, Theoret. Appl. Fract. Mech. 31 (1999) 47.

[5] V. Gupta, M. O'Brien, A.N. Pronin, J. de Phys. IV 9 (1999) 305.

[6] D.C. Agrawal, R. Raj, Mater. Sci. Engng. A 126 (1990) 125.

[7] J.-L. Houpert, S.L. Phoenix, R. Raj, Acta Metal. et Mater. 42 (1994) 4177.

[8] M.G. Cain, A.M. Danial, M.H. Lewis, Mater. Lett. 17 (1993) 246.

[9] G. Dehm, M. Ruhle, H.D. Conway, R. Raj, Acta Mater. 45 (1997) 489.

[10] D. Rouby, in: R.C. Bradt, D.P.H. Hasselman, D. Munz, M. Sakai, et al. (Eds.), Fracture Mechanics of Ceramics, Fatigue, Composites, and High-Temperature Behavior, vol. 12, New York, Plenum Press, 1996, pp. 229–252.

[11] N.C. Alstrup, N. Langvad, I. Chorkendorff, Surf. Interf. Anal. 23 (1995) 779.

[12] S.K. Venkataraman, D.L. Kohlstedt, W.W. Gerberich, Thin Solid Films 223 (1993) 269.

[13] S.K. Venkataraman, J.C. Nelson, A.J. Hsieh, D.L. Kohlstedt, et al., J. Adhes. Sci. Technol. 7 (1993) 1279.

[14] R.M. Pilliar, J. Nutting, Phil. Mag. 16 (1967) 181.

[15] B.J. Dalgleish, E. Saiz, A.P. Tomsia, R.M. Cannon, R.O. Ritchie, Scripta Metall. Mater 31 (1994) 1109.

[16] V. Stamos, S.D. Peteves, V. Kostopoulos, Engng. Fract. Mech. 60 (1998) 323.

[17] V. Gupta, A. Pronin, J. Am. Ceram. Soc. 78 (1995) 1397.

[18] J.T. Ranney, D.E. Starr, J.E. Musgrove, D.J. Bald, C.T. Campbell, Faraday Disciss. 114 (1999) 195.

[19] I.A. Ashcroft, B. Derby, J. Mater. Sci. 28 (1993) 2989.

[20] A. Christensen, E.A.A. Jarvis, E.A. Carter, Atomic-level properties of thermal barrier coatings: characterization of metal–ceramic interfaces, in: R.A. Dressler, C. Ng (Eds.), Chemical Dynamics in Extreme Environments, vol. 11, Advanced Series in Physical Chemistry, World Scientific, Singapore, 2001, pp. 490–546.

[21] A. Christensen, E.A. Carter, Phys. Rev. B 62 (2000) 16968.

[22] A. Christensen, E.A. Carter, J. Chem. Phys. 114 (2001) 5816.

[23] E.A.A. Jarvis, E.A. Carter, J. Phys. Chem. 105 (2001) 4045.

[24] E.A.A. Jarvis, R.L. Hayes, E.A. Carter, Chem. Phys. Chem. 2 (2001) 55.

[25] E. Ryshkewitch, D.W. Richerson, Oxide Ceramics, Academic Press, Orlando, 1985.

[26] J.A. Haynes, E.D. Rigney, M.K. Ferber, W.D. Porter, Surf. Coat. Technol. 86/87 (1996) 102.

[27] D. Zhu, R.A. Miller, in: D.A. Shores, R.A. Rapp, P.Y. Hou (Eds.), Fundamental Aspects of High Temperature Corrosion, Electrochemical Society, Pennington, 1997, pp. 289–307.

[28] D. Zhu, L.J. Ghosn, R.A. Miller, in: P.Y. Hou, M.J. McNallan, R. Oltra, E.J. Opila, et al. (Eds.), Proceedings of the Symposium on High Temperature Corrosion and Materials Chemistry, Electrochemical Society, Pennington, 1998, pp. 170–189.

[29] W. Brandl, D. Toma, H.J. Grabke, Surf. Coat. Technol. 108/109 (1998) 10.

[30] B.A. Pint, I.G. Wright, W.Y. Lee, Y. Zhang, K. Prüßner, K.B. Alexander, Mater. Sci. Engng. A 245 (1998) 201.

[31] A.M. Freborg, B.L. Ferguson, W.J. Brindley, G.J. Petrus, Mater. Sci. Engng. A 245 (1998) 182.

[32] K. Wefers, G.M. Bell, Tech. Report No.19, Alcoa Research Labs, Pittsburgh, PA, 1972, p. 37–43.

[33] E.M. Clausen Jr., J.J. Hren, The gamma to alpha transformation in thin film alumina, Mat. Res. Soc. Symp. Proc. 41 (1985) 381.

[34] I. Manassidis, A. De Vita, M.J. Gillan, Surf. Sci. Lett. 285 (1993) L517.

[35] I. Manassidis, M.J. Gillan, J. Am. Ceram. Soc. 77 (1994) 335.

[36] W.C. Mackrodt, R.J. Davey, S.N. Black, J. Crystal Growth 80 (1987) 441.

[37] S.M. Wiederhorn, J. Am. Ceram. Soc. 52 (1969) 485.

[38] C.A.M. Mulder, J.T. Klomp, J. Phys. Coll. 46 (1985) 111.

[39] P. Drillet, Doctorate Thesis, University of Rennes, France, 1991.

[40] C. Wan, M. Dupeux, J. Mater. Sci. 28 (1993) 5079.

[41] J.T. Klomp, Ceramic–metal interactions, Mater. Res. Soc. Symp. Proc. 40 (1985) 381.

[42] M. Humenik, W.D. Kingery, J. Am. Ceram. Soc. 37 (1954) 18.

[43] R. Brydson, H. Mullejans, J. Bruley, P.A. Trusty, X. Sun, J.A. Yeomans, M. Ruhle, J. Micros. 177 (1995) 369.

[44] S. Subramanian, S.L. Sass, J. Chinese Institute Engineers 21 (1998) 633 and references therein.

[45] Q. Zhong, F.S. Ohuchi, J. Vac. Sci. Technol. A 8 (1990) 2107.

[46] J.A. Wasyncznk, M. Rühle, Ceramic Microstructure '86: Role of Interfaces, Plenum, New York, 1987, p. 341.

[47] K. Kishitake, H. Era, F. Otsubo, T. Sonoda, J. Therm. Spray Technol. 7 (1998) 64.

[48] M.W. Finnis, Acta Metall. Mater. 40 (1992) S25.

[49] M.W. Finnis, J. Phys.: Condens. Matter 8 (1996) 5811.

[50] F. Ernst, Mater. Sci. Engng. R 14 (1995) 97.

[51] M.Y. He, A.G. Evans, J.W. Hutchinson, Mater. Sci. Engng. A 245 (1998) 168.

[52] M. Finot, S. Suresh, C. Bull, A.E. Giannakopoulos, et al., Experimental studies of thermal cycling of a Ni–Al$_2$O$_3$ graded material, in: B. Ilschner, N. Cherradi (Eds.) 3rd International Symposium on Structural and Functional Gradient Materials, 1995, p. 229.

[53] K.H. Johnson, S.V. Pepper, J. Appl. Phys. 53 (1982) 6634.

[54] A.B. Andersen, S.P. Mehandru, J.L. Smialek, J. Electrochem. Soc. 132 (1985) 1695.

[55] A.D. Zdetsis, A.B. Kunz, Phys. Rev. B 32 (1985) 6358.

[56] F. Raatz, D.R. Salahub, Surf. Sci. 156 (1985) 982.

[57] B.C. Lippens, Structure and Texture of Aluminas, Thesis, Technische Hogeschool of Delft, The Netherlands, 1961, p. 85.

[58] G. Pacchioni, N. Rosch, Surf. Sci. 306 (1994) 169.

[59] C. Kruse, M.W. Finnis, V.Y. Milman, M.C. Payne, A. De Vita, M.J. Gillan, J. Am. Ceram. Soc. 77 (1994) 431.

[60] C. Kruse, M.W. Finnis, J.S. Lin, M.C. Payne, V.Y. Milman, A. De Vita, M.J. Gillan, Phil. Mag. Lett. 73 (1996) 377.

[61] I.G. Batirev, A. Alavi, M.W. Finnis, T. Deutsch, Phys. Rev. Lett. 82 (1999) 1510.

[62] C. Verdozzi, D.R. Jennision, P.A. Shultz, M.P. Sears, Phys. Rev. Lett. 82 (1999) 799.

[63] A. Bogicevic, D.R. Jennison, Phys. Rev. Lett. 82 (1999) 4050.

[64] D.R. Jennision, C. Verdozzi, P.A. Shultz, M.P. Sears, Phys. Rev. B 59 (1999) R15605.

[65] D.R. Jennision, A. Bogicevic, Faraday Discuss. 114 (1999) 45.

[66] D.R. Jennision, A. Bogicevic, Surf. Sci. 464 (2000) 108.

[67] A.Y. Lozovoi, A. Alavi, M.W. Finnis, Phys. Rev. Lett. 85 (2000) 610.

[68] P. Hohenberg, W. Kohn, Phys. Rev. B 136 (1964) 864.

[69] W. Kohn, L.J. Sham, Phys. Rev. A 140 (1965) 1133.

[70] G. Kresse, J. Hafner, Phys. Rev. B 47 (1993) 558.

[71] G. Kresse, J. Hafner, Phys. Rev. B 49 (1994) 14251.

[72] G. Kresse, J. Furthmuller, Comput. Mater. Sci. 6 (1996) 15.

[73] D. Vanderbilt, Phys. Rev. B 41 (1990) 7892.

[74] G. Kresse, J. Hafner, J. Phys.: Condens. Matter 6 (1994) 8245.

[75] J.P. Perdew, Phys. Rev. B 33 (1986) 8822, 34 (1986) 7406(E).

[76] J.P. Perdew, in: P. Ziesche, H. Eschrig (Eds.), Electronic Structure of Solids, Akademie Verlag, Berlin, 1991, p. 11.

[77] L. Kleinman, D.M. Bylander, Phys. Rev. Lett. 48 (1982) 1425.

[78] A.M. Rappe, K.M. Rabe, E. Kaxiras, J.D. Joannopoulos, Phys. Rev. B 41 (1990) 1227.

[79] J.P. Perdew, A. Zunger, Phys. Rev. B 23 (1981) 5048.

[80] S. Nosé, J. Chem. Phys. 81 (1984) 511.

[81] S. Nosé, Prog. Theor. Phys. Suppl. 103 (1991) 1.

[82] P.E. Blöchl, O. Jepsen, O.K. Andersen, Phys. Rev. B 49 (1994) 16223.

[83] M. Methfessel, A.T. Paxton, Phys. Rev. B 40 (1989) 3616.

[84] J. Lewis, D. Schwarzenbach, H.D. Flack, Acta Cryst. A 38 (1982) 733.

[85] Y.-N. Xu, W.Y. Ching, Phys. Rev. B 43 (1991) 4461.

[86] G. Pacchioni, C. Sousa, F. Illas, F. Parmigiani, P.S. Bagus, Phys. Rev. B 48 (1993) 11573.

[87] W.Y. Ching, Y.-N. Xu, J. Am. Ceram. Soc. 77 (1994) 404.

[88] G. Kresse, D. Joubert, Phys. Rev. B 59 (1999) 1758.

[89] C. Kittel, Introduction to Solid State Physics, sixth ed., Wiley, New York, 1986.

[90] F.D. Murnaghan, Proc. Nat. Acad. Sci. 30 (1944) 2344.

[91] K.T. Thomson, R.M. Wentzcovitch, M.S.T. Bukowinski, Science 274 (1996) 1880.

[92] J. Guo, D.E. Ellis, D.J. Lam, Phys. Rev. B 45 (1992) 13647.

[93] A. Wander, B. Searle, N.M. Harrison, Surf. Sci. 458 (2000) 25.

[94] M. Causá, R. Dovesi, C. Pisani, C. Roetti, Surf. Sci. 215 (1989) 259.

[95] P.W. Tasker, Advances in Ceramics 10, in: W.D. Kingery (Ed.), 1984, p. 176.

[96] S. Blonski, S.H. Garofalini, Surf. Sci. 295 (1993) 263.

[97] V.E. Puchin, J.D. Gale, A.L. Shluger, E.A. Kotomin, J. Gunster, M. Brause, V. Kempter, Surf. Sci. 370 (1997) 190.

[98] A. Chame, F. Lancon, P. Paliti, G. Renaud, I. Vilfan, J. Villain, Int. J. Mod. Phys. B 11 (1997) 3657.

[99] S.K. Rhee, J. Am. Ceram. Soc. 55 (1972) 300.

[100] L. Vitos, A.V. Ruban, H.L. Skriver, J. Kollar, Surf. Sci. 411 (1998) 186.

[101] W.R. Tyson, W.A. Miller, Surf. Sci. 62 (1977) 267.

[102] F.R. de Boer, R. Boom, W.C.M. Mattens, A.R. Miedema, A.K. Niessen, Cohesion in Metals, North-Holland, Amsterdam, 1988.

[103] J.C. Fuggle, F.U. Hillebrecht, R. Zeller, Z. Zolnierek, P.A. Bennett, C. Freiburg, Phys. Rev. B 27 (1982) 2145.

[104] K.-H. Hellwege, A.M. Hellwege, Group III, 7b1 (Eds.), Landolt-Börnstein Tables, Springer, Berlin, 1975.

[105] W.B. Person, A Handbook of Lattice Spacing and Structures of Metals and Alloys, Pergamon, Oxford, 1958.

[106] F.X. Kayser, C. Stassis, Phys. Stat. Sol. A 64 (1981) 335.

[107] A.D. Becke, K.E. Edgecombe, J. Chem. Phys. 92 (1990) 5397.

[108] B. Silvi, A. Savin, Nature 371 (1994) 683.

[109] A. Savin, O. Jepsen, J. Flad, O.K. Andersen, H. Preuss, H.G. von Schneiring, Angew. Chem. Int. Engl. 31 (1992) 187.

[110] L. DeSantis, R. Resta, Surf. Sci. 450 (2000) 126.

[111] P.H.M. de Korte, E.B.M. Doesburg, C.P.J. de Winter, L.L. van Reijen, Solid State Ionics 16 (1985) 73.

[112] J.A. Haynes, M.K. Ferber, W.D. Porter, E.D. Rigney, Oxidation of Metals 52 (1999) 31.

[113] J.A. Haynes, M.K. Ferber, W.D. Porter, E.D. Rigney, Mater. High Temp. 16 (1999) 49.

[114] J.A. Haynes, M.K. Ferber, W.D. Porter, in: P.Y. Hou, M.J. McNallan, R. Oltra, E.J. Opila, et al. (Eds.), Proceedings of the Symposium on High Temperature Corrosion and Materials Chemistry, Electrochemical Society, Pennington, 1998, p. 146–157.

[115] K.G. Schmitt-Thomas, M. Hertter, Surf. Coat. Tech. 120/121 (1999) 84.

[116] C.R.A. Catlow, R. James, W.C. Mackrodt, R.F. Stewart, Phys. Rev. B 25 (1982) 1006.

[117] B.G. Dick, A.W. Overhauser, Phys. Rev. 112 (1958) 90.

[118] W.C. Mackrodt, R.F. Stewart, J. Phys. C 12 (1979) 431.